

LETTERS

Efficient quantum memory for light

Morgan P. Hedges¹, Jevon J. Longdell², Yongmin Li³ & Matthew J. Sellars¹

Storing and retrieving a quantum state of light on demand, without corrupting the information it carries, is an important challenge in the field of quantum information processing. Classical measurement and reconstruction strategies for storing light must necessarily destroy quantum information as a consequence of the Heisenberg uncertainty principle. There has been significant effort directed towards the development of devices—so-called quantum memories—capable of avoiding this penalty. So far, successful demonstrations^{1–6} of non-classical storage and on-demand recall have used atomic vapours and have been limited to low efficiencies, of less than 17 per cent, using weak quantum states with an average photon number of around one. Here we report a low-noise, highly efficient (up to 69 per cent) quantum memory for light that uses a solid-state medium. The device allows the storage and recall of light more faithfully than is possible using a classical memory, for weak coherent states at the single-photon level through to bright states of up to 500 photons. For input coherent states containing on average 30 photons or fewer, the performance exceeded the no-cloning limit. This guaranteed that more information about the inputs was retrieved from the memory than was left behind or destroyed, a feature that will provide security in communications applications.

A quantum memory for light is a device that reversibly maps the quantum information in a light field to the quantum state of a material system, making possible its recall on demand. The basic role of the memory is to allow the synchronization of different processes in quantum information applications. By avoiding measurement of the input state, a quantum memory may circumvent the Heisenberg uncertainty principle, preserving delicate quantum information that would otherwise be destroyed. Preserving this information is of fundamental importance for quantum information applications.

The first demonstration of a one-way mapping of light onto a material more faithfully than can be achieved classically was demonstrated in 2004⁷. Since then, there have been a number of demonstrations of quantum memory processes with on-demand retrieval. The quantum nature of these memories was shown by characterization using coherent input states³ and by the preservation of quantum behaviour for non-classical inputs^{1,2,4–6}. The highest reported recall efficiency of these demonstrations was 17% (ref. 5). In addition, high-fidelity light–matter interfaces with potential for on-demand recall have been recently demonstrated using solid-state media⁸.

For practical quantum information applications such as quantum networks, the development of memories with substantially higher efficiencies will be necessary to allow long-distance (for example >1,000 km) quantum communication to occur with practical transmission rates⁹. Furthermore, attaining an efficiency of 50% represents a fundamental benchmark that is critical for many applications. An efficiency above 50% is a necessary condition for a memory to operate within the no-cloning regime without post-selection¹⁰, and

it is the level at which error correction protocols that counter qubit loss become available in linear-optics quantum computing¹¹.

Quantum memory schemes form a subset of coherent optical memory techniques, that is, techniques that preserve conjugate variables of their inputs. A quantum memory is a coherent memory that performs well enough to preserve quantum information of an unknown state. Coherent techniques include electromagnetically induced transparency¹², off-resonance Raman interaction¹³, the use of atomic frequency combs⁸ and gradient echoes¹⁴. So far, the highest reported efficiency for a coherent memory is 45% (refs 15, 16). We make no distinction here between continuous- and discrete-variable storage, as the linearity of these techniques means they may work equally well for both, and indeed a quantum process is completely characterized by its effect on the set of coherent states³.

These coherent memory techniques involve mapping the state of the light onto ensembles of absorbers. They have been implemented in warm atomic vapours, ultracold atomic gases and rare-earth ions doped into crystals. These systems are related in their use of high optical dispersion and, thus, in their requirement of a high spectral density of absorbers. The optical transitions of rare-earth ions in solids can satisfy these criteria owing to their high degree of isolation from their environment. These ions maintain long coherence times both for their optical¹⁷ and spin¹⁸ transitions even when closely packed in a solid. As a result, some of the highest efficiencies¹⁶, as well as the longest storage time yet reported¹⁸ for any of these coherent memory techniques, have been realized using such ions. These recent achievements are in part attributable to the extensive investigations into rare-earth-doped crystals for classical information storage and processing¹⁹.

The optical gradient-echo memory^{14,20}, the optical analogue of the gradient echo used in nuclear magnetic resonance, is also referred to as a ‘longitudinal’ variant of controlled reversible inhomogeneous broadening²¹. An optical gradient echo is a linear process capable of multimode storage with efficiencies approaching 100%, and is extendable to a lambda system to obtain long-term storage in spin states^{22,23}. The scheme has been shown to remain linear down to the single-photon level²⁴. It is theoretically predicted to be noise free; however, until now the scheme’s low noise has not been verified experimentally. An important advantage of a gradient-echo memory over other coherent memories is that it is not necessarily limited in bandwidth by hyperfine structure²⁵.

Echo techniques such as this may be understood in terms of the reciprocal nature of coherent absorption and emission. To absorb an incident radiant pulse, absorbers in an optically thick medium may be thought of as radiating an equal-but-opposite cancelling pulse, such that the net radiation leaving the medium is zero. Echo techniques reverse the evolution of these absorbers to recreate the conditions of absorption, such that the medium re-emits this cancelling pulse in the absence of the original. Situations can be engineered^{14,21,26} in which this ‘echo’ contains all the information of the original pulse.

¹Laser Physics Centre, Research School of Physics and Engineering, Australian National University, Canberra, Australian Capital Territory 0200, Australia. ²Jack Dodd Centre, Physics Department, University of Otago, Dunedin 9016, New Zealand. ³State Key Laboratory of Quantum Optics and Quantum Optics Devices, Institute of Opto-Electronics, Shanxi University, Taiyuan 030006, China.

In a gradient echo, the evolution of the absorbers is controlled using an externally applied field. An initial, spectrally narrow absorption feature is detuned as a linear function of propagation depth (a detuning ‘gradient’) to effectively create a broad feature. An echo of radiation absorbed by this broad feature is created by reversing the detuning gradient, effectively reversing the relative evolution of the absorbers. The spectral profile of the initial feature is crucial to performance, with efficiency and storage time scaling with its spectral sharpness and optical thickness.

Initial demonstrations of an optical gradient echo used persistent spectral hole-burning to create a narrow feature in the broad inhomogeneous lines of $\text{Eu}^{3+}:\text{Y}_2\text{SiO}_5$ (ref. 20) and $\text{Pr}^{3+}:\text{Y}_2\text{SiO}_5$ (ref. 14), with the detuning gradient created using the linear Stark shift and an electric field gradient. A similar experiment was recently performed at telecommunication wavelengths using $\text{Er}^{3+}:\text{Y}_2\text{SiO}_5$ (ref. 24). Other recent demonstrations have used a Raman feature in warm rubidium vapour and the linear Zeeman shift²³. This system was also used to demonstrate coherent pulse sequencing and manipulation²⁷.

In the present work, we solve the major problem faced in early experiments^{14,20}, that of creating a highly absorbing, yet spectrally very sharp, absorption feature in a highly transmissive spectral window. We do this by using novel hole-burning techniques and a long, lightly doped Pr^{3+} (0.005%): Y_2SiO_5 single crystal. Furthermore, we select for ions with the same sign and magnitude of Stark shift as is necessary for a pure gradient-echo protocol and high efficiency²⁸. Using this improved spectral feature and quantum-noise-limited, phase-sensitive detection, we are able to measure the noise characteristics of the gradient-echo process for both weak and bright coherent inputs, in the high-efficiency regime.

The experiment is shown in Fig. 1. It was carried out on the $^3\text{H}_4 \leftrightarrow ^1\text{D}_2$ 605.98-nm optical transition of praseodymium ions in $\text{Pr}^{3+}:\text{Y}_2\text{SiO}_5$. The crystal was excited both along its length and from the side with light from a highly stabilized laser (linewidth, ~ 1 kHz). Light incident along the length of the crystal was measured using balanced heterodyne detection (Supplementary Information) was used to create a spectral feature

with 140 dB peak absorption and 140 kHz width within the a 14-mm length of crystal, with average background levels of 0.1 dB on the low-frequency side and 2.5 dB on the high-frequency side. An absorption spectrum of a pulse transmitted through this feature shows some of its properties (Fig. 2b), although this measurement is limited in its dynamic range. Figure 2c shows the same measurement when a +20-V potential applied to the front and back electrodes has broadened the feature to 1.6 MHz, representing the memory’s bandwidth. The polarity of the Stark shift, selected through hole-burning, and of the field gradient, was such that the ions towards the input side of the crystal were detuned to higher frequency, whereas those towards the output were detuned to lower frequency.

Temporally Gaussian pulses of coherent light with an intensity full-width at half-maximum of 0.6 μs were absorbed by this broadened feature and then recalled by switching the electrodes to -20 V in <150 ns. The measurements presented in Fig. 2 indicate that the storage was $69 \pm 2\%$ efficient, measured on the basis of pulse energy, after storage for 1.3 μs . After a storage time of 2.6 μs , the efficiency was found to be $45 \pm 2\%$, indicating a decay time for the storage of 3 μs , although the decay is not strictly exponential owing to the non-Lorentzian initial feature. The echo efficiency was found to be highly sensitive to the spectrum of the initial feature, but only to its low-frequency side. This is expected, as the depth–detuning correlation in a gradient echo means that only one side of the optically thick feature interacts with the light²⁵.

An established theoretical model¹⁴ based on the Maxwell–Bloch equations, modified to include the inhomogeneous line shape of the initial feature (Fig. 2b), was used to simulate the echo amplitude and found to be in good agreement with that observed. The initial feature was modelled as that from a 14-mm-long interaction region with a spectral profile given by a 140-kHz-wide ‘top-hat’ distribution convolved with a Lorentzian of half-width 12 kHz at the edges. The peak absorption was ~ 100 dB cm^{-1} and the background absorption was 0.06 dB cm^{-1} on the low-frequency side and 1.8 dB cm^{-1} on the high-frequency side. The electric field used in the simulation (Fig. 1, inset) was that determined from a finite-element model of

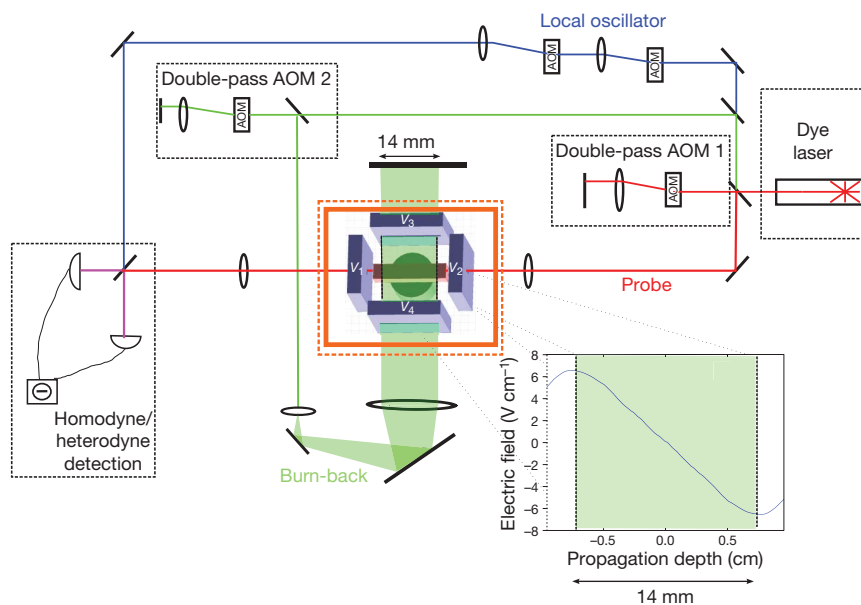


Figure 1 | Experimental set-up. Light from a highly stabilized dye laser, gated by acousto-optic modulators (AOMs), is directed at a 2-cm-long $\text{Pr}:\text{Y}_2\text{SiO}_5$ crystal mounted between Teflon plates, surrounded by four copper block electrodes with holes to allow the beams through. The crystal and holder are held in a liquid helium cryostat at 3 K. The memory is prepared by first burning a spectral trench over the full length of the crystal using the forward beam, then burning back a feature in the central 14 mm using a beam from the side. This side excitation avoided propagation effects and allowed the feature to be created only in the centre of the crystal, where

the electric gradient field was monotonic. Inset, the component of the electric field along the propagation axis as determined by finite-element modelling of the holder, including the dielectric constant of the crystal and its Teflon mount. The shaded region represents the length over which the feature was created. The field gradient was created by grounding V_3 and V_4 and applying 20 V to V_1 and V_2 . The gradient was switched by changing this to -20 V. V_3 and V_4 were used in the preparation sequence, as described in Supplementary Information.

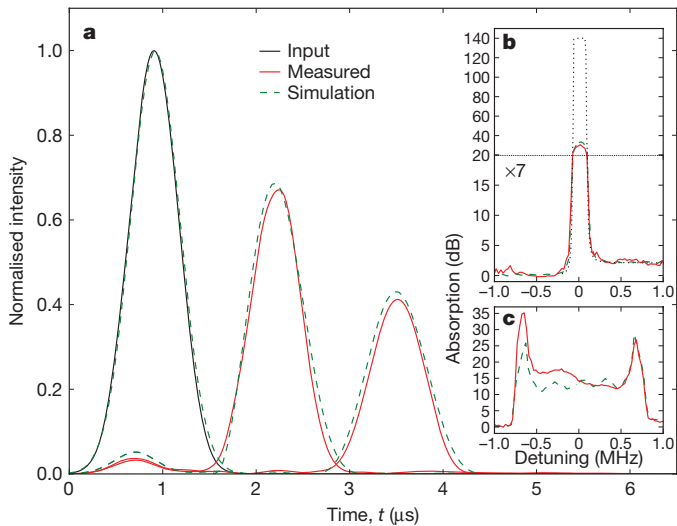


Figure 2 | Efficiency and spectral measurements. Measured and simulated data showing the obtained echoes and the corresponding absorption spectra. The simulations were based on Maxwell–Bloch equations. The input pulse was calibrated by measuring the transmission of a pulse through the transmissive spectral trench before every experiment. This trench was measured to be $<2\%$ absorbing using separate measurements with the laser far off resonance. The uncertainty in this measurement is taken into account in quoted efficiencies. **a**, Input and retrieved pulses. The field begins switching at $t = 1.4 \mu\text{s}$ for the first retrieved pulse and at $t = 2.0 \mu\text{s}$ for the second. In the case of no field switch, 97% of the input pulse energy is absorbed. **b**, Absorption spectrum of the prepared feature measured by transmission of a short pulse. The dynamic range of the measurement was insufficient to resolve the peak absorption of the feature, which was confirmed by independent measurements on shorter interaction lengths to be 100 dB cm^{-1} . The black dotted trace represents a perfect measurement of the feature used in the simulations. **c**, Absorption spectrum when the field was not switched to retrieve the pulse, that is, with 20 V applied to the end electrodes. The Stark shift of the ions is such that their resonant frequency is negatively correlated with their depth. This means that the higher-frequency side of this spectrum is due to ions towards the input end of the crystal and that the low-frequency side is due to those towards the output end. The simulation used the electric field determined in the inset of Fig. 1.

the crystal and sample holder. The absorption spectrum of the broadened feature (Fig. 2b) was not shaped like a top hat in profile, owing mainly to the nonlinear field gradient. The asymmetry of the measured broadened feature was due to real variations in the peak absorption along the length of the crystal, a characteristic that was not accounted for in the simulation.

To measure the noise performance of the memory, we repeated the experiment 5,000–10,000 times with different input intensities corresponding to pulses with photon number expectation values, $\langle N \rangle$, of between ~ 1 and $\sim 10^4$. Homodyne quadrature measurements were made on the input and retrieved modes while the relative phase of the local oscillator was allowed to vary between 0 and 2π . We measured this phase using relatively intense reference pulses offset in frequency by -2.5 MHz , before and after each measurement, with a precision of 30 mrad . Slow classical intensity fluctuations of the laser caused 0.05% noise in the input and retrieved modes, contributing noise of $\sim 0.1\%$ in units of the vacuum-state variance relative to the mean photon number in the mode. This became significant for states with $\langle N \rangle > 100$. To avoid noise due to electrical pickup in the detectors caused by the fast-switching electric field, a storage time of $1.6 \mu\text{s}$ was used for these measurements, and in this case an efficiency of $61 \pm 2\%$ was observed. Representative examples of this data are shown in Fig. 3a–d.

We fitted the data to a general normalized mode of the electric field with quadrature expectation value at measurement phase θ given by $\langle X_\theta \rangle = X_0 \sin(\theta - \theta_0)$ and variance given by²⁹

$$V_\theta = V_x \sin^2(\theta - \theta_0) + V_p \cos^2(\theta - \theta_0) - V_{xp} \sin^2(\theta - \theta_0)$$

The parameters for amplitude, X_0 ; phase, θ_0 ; amplitude variance, V_x ; phase variance, V_p ; and noise cross-coupling, V_{xp} ; and their uncertainties, were found for each data set by maximum-likelihood estimation, using an adaptive Metropolis algorithm³⁰ and assuming Gaussian noise. The parameters of the state directly after the sample were calculated by accounting for losses due to optical attenuation, detector inefficiency and mode mismatch (total 41%), as well as electrical noise due to the detectors and electrical pickup from the field switch. The four input states were found to have respective photon numbers $\langle N \rangle \approx |X/2|^2 = 4, 30, 500$ and $19,000$.

Figure 3e–h shows the additional variance, V_{add}^θ , introduced by the memory process as a function of θ , in units of the vacuum-state variance. To account for a significant level of classical noise in the larger ($\langle N \rangle = 500$ and $19,000$) input states, the noise levels of the retrieved states were compared with that of the input after its classical noise had been attenuated by the memory efficiency. Specifically, the expected variance is $V_{\text{att}}^\theta = \eta V_{\text{in}}^\theta + 1 - \eta$, where V_{in}^θ is the variance measured for the input state and η is the memory efficiency. For the two lower-intensity states, this correction was insignificant and not required. The memory's effect on the input can be compared with two relevant benchmarks for the preservation of conjugate amplitude quadratures: the performance of a classical memory based on ideal measurements, and that of an ideal $1 \rightarrow 2$ cloning device¹⁰. In terms of the added variance, it can be shown that a coherent memory will perform better than the first benchmark if $V_{\text{add}}^\theta \leq 2\eta$ and better than the second if $V_{\text{add}}^\theta \leq 2\eta - 1$, for all θ (Supplementary Information).

From Fig. 3, it is seen that the $\langle N \rangle = 4$ and $\langle N \rangle = 30$ states were retrieved with the addition of less noise than allowed for by the classical and no-cloning limits, over all phases. The $\langle N \rangle = 500$ state shows little added noise in the amplitude quadrature; however, ~ 0.5 units in the phase quadrature have been introduced. This state was stored and recalled more faithfully than in the classical limit, but it is not clear whether it was in the no-cloning regime. The data on the $\langle N \rangle = 19,000$ state also do not indicate added noise in the amplitude quadrature, but do show 18 vacuum units added to the phase quadrature. For this state, it is clear that the storage is worse than in both limits. As with the $\langle N \rangle = 500$ state, the added noise in the phase quadrature is dominant. The additional variance observed in the phase quadrature seems to be linear in $\langle N \rangle$ with a constant of proportionality of 10^{-3} . It is consistent with a slight distortion of the large pulses used as phase references varying over the course of these measurements as a result of spectral hole-burning.

The simulated results are in good agreement with the observed echoes, and it is therefore reasonable to use the model to consider optimizing the memory's efficiency. Increasing the interaction length of the crystal to 4 cm, with no other change, is predicted to increase the efficiency of the first retrieved pulse to 88%. Increasing the length of the crystal beyond 4 cm will begin to decrease the efficiency owing to increasing background absorption. Improvements in the preparation sequence should potentially reduce this background by an order of magnitude. In the case of negligible background absorption, the model predicts that efficiencies approaching 96% could be achieved with sample lengths greater than 10 cm. In this regime, the efficiency is limited by the spontaneous lifetime of the optical transition and the finite duration of the stored pulse. Further increases in efficiency and the time–bandwidth product are predicted to require the storage of shorter pulses and, thus, greater memory bandwidth. The prospects for achieving this are discussed below.

In the current implementation, the maximum bandwidth achievable is limited by the hyperfine structure to $\sim 10 \text{ MHz}$. This is because spectral hole-burning cannot be used to create a good transmissive window that is wider than the smallest splitting between hyperfine levels. This limitation may be removed by reducing the inhomogeneous broadening in the crystal to below the level of the hyperfine splittings. In this case, the highest or lowest energy transition among the levels will have a

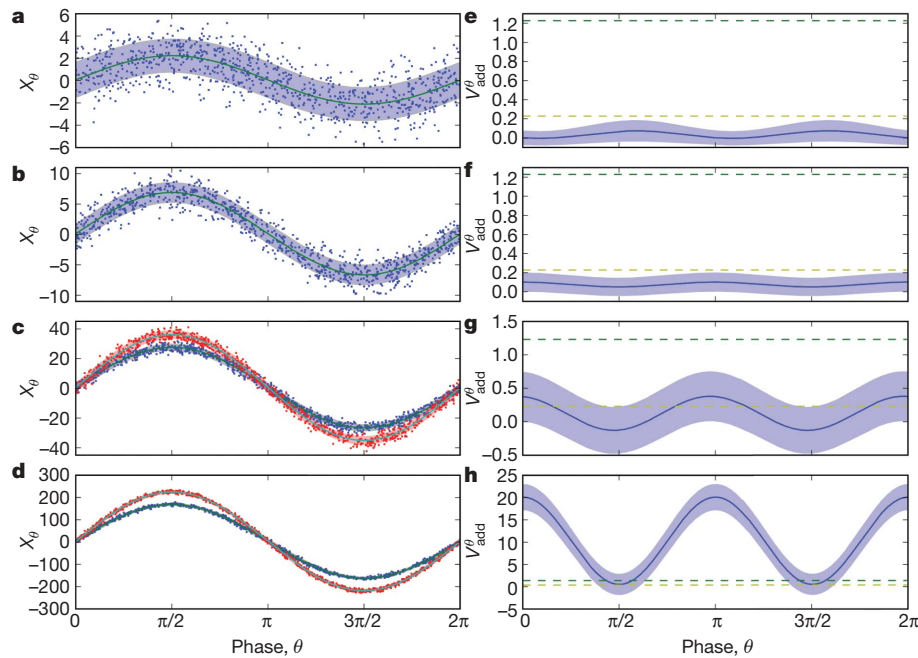


Figure 3 | Noise due to the memory and comparison with benchmarks. **a–d**, Sets of 1,000 obtained quadrature values versus phase of the local oscillator for stored pulses (blue dots), in units of vacuum noise. The pulses had respective mean photon numbers of $\langle N \rangle = 4$ (**a**), 30 (**b**), 500 (**c**) and 19,000 (**d**). For the $\langle N \rangle = 500$ and 19,000 data sets, the quadrature values of the input pulses are also shown (red dots). The green line and blue band respectively represent the mean amplitude and standard deviation of the Gaussian state fit to the corresponding set of retrieved data. The cyan line and pink band represent the same for the $\langle N \rangle = 500$ and $\langle N \rangle = 19,000$ input

states. **e–h**, The blue line represents noise introduced by the memory, in units of the vacuum variance, for the four input states: $\langle N \rangle = 4$ (**e**), 30 (**f**), 500 (**g**) and 19,000 (**h**). Here the blue band indicates the $68 \pm 1\%$ (s.d.) confidence interval in our determination of the added variance as a function of phase. The dashed dark and light green lines indicate the performance of an ideal phase-insensitive classical memory and a symmetrical $1 \rightarrow 2$ state-cloning device, respectively. For all the retrieved quadrature values, a 50-kHz frequency shift and $5\pi/6$ phase shift relative to the input mode have been accounted for.

completely free transmissive window on its higher-frequency or, respectively, lower-frequency side. A gradient-echo memory could take advantage of this essentially semi-infinite window because the correlation between propagation depth and frequency may be used to hide the remaining hyperfine structure, which will be entirely on the higher-frequency (or lower-frequency) side of the initial feature. In this case, in which the hyperfine splittings are greater than the inhomogeneous broadening, the memory bandwidth and efficiency are limited only by the optical depth of the transition and the magnitude of the Stark (or other detuning) gradient that can be applied.

Such a hyperfine-resolved spectrum will also greatly simplify the implementation of long-lived spin storage of the light. In the present experiment, the memory storage time is limited by the short coherence time of the high-energy electronic transition used. Long-lived storage is achieved by transferring the information in the optical transition to a ground-state transition associated with long-lived nuclear spin. This adds a constraint that the optical transitions of the ions in the initial ensemble be between particular hyperfine levels²². In crystals with high inhomogeneous broadening, this significantly reduces the number and spectral density of ions that can be used and, hence, the efficiency of the memory. In comparison, for a crystal with resolved structure every ion in the crystal could be optically pumped into the same hyperfine ground state. In this situation, the potential efficiency of the long-lived spin storage (three-level) memory will be the same as for the electronic storage (two-level) memory, and may approach the theoretical limits of both as every ion in the crystal may contribute to the storage.

There is a realistic prospect of achieving such low inhomogeneous broadening and at the same time increasing the optical depth through the use of isotropically pure, stoichiometric rare-earth crystals such as $\text{EuCl}_3 \cdot 6\text{H}_2\text{O}$ (ref. 25). The much greater optical depth and absence of structural-bandwidth limitations in such materials promises much greater efficiency and higher multimode capacity than in

the implementation here. Furthermore, the spin storage times in $\text{EuCl}_3 \cdot 6\text{H}_2\text{O}$ are predicted to be significantly longer than the 2.3-s storage time demonstrated using electromagnetically induced transparency in $\text{Pr}^{3+}:\text{Y}_2\text{SiO}_5$ (ref. 31). With realistic material improvements along these lines, using a gradient echo with spin storage^{22,23}, it should be feasible to achieve the stringent requirements for a practical quantum memory, with multimode storage on the timescale of seconds, $>90\%$ efficiency and $>1\text{-GHz}$ bandwidth⁹.

Received 9 January; accepted 13 April 2010.

1. Appel, J., Figueroa, E., Korystov, D., Lobino, M. & Lvovsky, A. Quantum memory for squeezed light. *Phys. Rev. Lett.* **100**, 093602 (2008).
2. Chanelière, T. *et al.* Storage and retrieval of single photons transmitted between remote quantum memories. *Nature* **438**, 833–836 (2005).
3. Lobino, M., Kupchak, C., Figueroa, E. & Lvovsky, A. I. Memory for light as a quantum process. *Phys. Rev. Lett.* **102**, 203601 (2009).
4. Eisaman, M. D. *et al.* Electromagnetically induced transparency with tunable single-photon pulses. *Nature* **438**, 837–841 (2005).
5. Choi, K., Deng, H., Laurat, J. & Kimble, H. Mapping photonic entanglement into and out of a quantum memory. *Nature* **452**, 67–71 (2008).
6. Honda, K. *et al.* Storage and retrieval of a squeezed vacuum. *Phys. Rev. Lett.* **100**, 093601 (2008).
7. Julsgaard, B., Sherson, J., Cirac, J. I., Fiurásek, J. & Polzik, E. S. Experimental demonstration of quantum memory for light. *Nature* **432**, 482–486 (2004).
8. de Riedmatten, H., Afzelius, M., Staudt, M. U., Simon, C. & Gisin, N. A solid-state light-matter interface at the single-photon level. *Nature* **456**, 773–777 (2008).
9. Sangouard, N., Simon, C., Riedmatten, H. D. & Gisin, N. Quantum repeaters based on atomic ensembles and linear optics. Preprint at (<http://arxiv.org/abs/0906.2699>) (2009).
10. Grosshans, F. & Grangier, P. Quantum cloning and teleportation criteria for continuous quantum variables. *Phys. Rev. A* **64**, 010301 (2001).
11. Varnava, M., Browne, D. & Rudolph, T. Loss tolerance in one-way quantum computation via counterfactual error correction. *Phys. Rev. Lett.* **97**, 120501 (2006).
12. Hau, L., Harris, S., Dutton, Z. & Behroozi, C. Light speed reduction to 17 metres per second in an ultracold atomic gas. *Nature* **397**, 594–598 (1999).
13. Nunn, J. *et al.* Mapping broadband single-photon wave packets into an atomic memory. *Phys. Rev. A* **75**, 011401 (2007).

14. Hétet, G., Longdell, J. J., Alexander, A. L., Lam, P. K. & Sellars, M. J. Electro-optic quantum memory for light using two-level atoms. *Phys. Rev. Lett.* **100**, 023601 (2008).
15. Novikova, I., Phillips, N. & Gorshkov, A. Optimal light storage with full pulse-shape control. *Phys. Rev. A* **78**, 021802 (2008).
16. Tittel, W. *et al.* Photon-echo quantum memory in solid state systems. *Laser Photon. Rev.* **4**, 244–267 (2009).
17. Böttger, T., Thiel, C., Cone, R. & Sun, Y. Effects of magnetic field orientation on optical decoherence in $\text{Er}^{3+}:\text{Y}_2\text{SiO}_5$. *Phys. Rev. B* **79**, 115104 (2009).
18. Longdell, J., Fraval, E., Sellars, M. & Manson, N. Stopped light with storage times greater than one second using electromagnetically induced transparency in a solid. *Phys. Rev. Lett.* **95**, 063601 (2005).
19. Sun, Y. Recent progress in developing new rare earth materials for hole burning and coherent transient applications. *J. Lumin.* **98**, 281–287 (2002).
20. Alexander, A. L., Longdell, J. J., Sellars, M. J. & Manson, N. B. Photon echoes produced by switching electric fields. *Phys. Rev. Lett.* **96**, 043602 (2006).
21. Kraus, B. *et al.* Quantum memory for nonstationary light fields based on controlled reversible inhomogeneous broadening. *Phys. Rev. A* **73**, 020302 (2006).
22. Alexander, A. L. *Investigation of Quantum Information Storage in Rare Earth Doped Materials*. PhD thesis, Australian National Univ. (2007).
23. Hétet, G. *et al.* Photon echoes generated by reversing magnetic field gradients in a rubidium vapor. *Opt. Lett.* **33**, 2323–2325 (2008).
24. Lauritzen, B. *et al.* Telecommunication-wavelength solid-state memory at the single photon level. *Phys. Rev. Lett.* **104**, 080502 (2010).
25. Ahlefeldt, R. L., Smith, A. & Sellars, M. J. Ligand isotope structure of the optical ${}^7\text{F}_0 \rightarrow {}^5\text{D}_0$ transition in $\text{EuCl}_3 \cdot 6\text{H}_2\text{O}$. *Phys. Rev. B* **80**, 205106 (2009).
26. Afzelius, M., Simon, C., de Riedmatten, H. & Gisin, N. Multimode quantum memory based on atomic frequency combs. *Phys. Rev. A* **79**, 052329 (2009).
27. Hosseini, M. *et al.* Coherent optical pulse sequencer for quantum applications. *Nature* **461**, 241–245 (2009).
28. Longdell, J., Hétet, G., Lam, P. & Sellars, M. Analytic treatment of controlled reversible inhomogeneous broadening quantum memories for light using two-level atoms. *Phys. Rev. A* **78**, 1–6 (2008).
29. Walls, D. & Milburn, G. *Quantum Optics* 20, 21 (Springer, 1994).
30. Haario, H., Saksman, E. & Tamminen, J. An adaptive Metropolis algorithm. *Bernoulli* **7**, 223–242 (2001).
31. Longdell, J., Alexander, A. & Sellars, M. Characterization of the hyperfine interaction in europium-doped yttrium orthosilicate and europium chloride hexahydrate. *Phys. Rev. B* **74**, 195101 (2006).

Supplementary Information is linked to the online version of the paper at www.nature.com/nature.

Acknowledgements The authors gratefully acknowledge S. Beavan, R. Ahlefeldt and J. Bartholomew for proofreading the manuscript. M.J.S. was supported by the Australian Research Council. J.J.L. was supported by a New Economy Research Fund grant from the New Zealand Foundation for Research Science and Technology

Author Contributions The initial project was conceived by M.J.S. and J.J.L. Various preliminary experiments were conducted by M.P.H. with assistance and guidance from M.J.S., J.J.L. and Y.L. The final experiment was designed, built and conducted by M.P.H. under the guidance of M.J.S. Data was analysed by M.P.H. with assistance in interpretation by M.J.S. and J.J.L. Theoretical modelling was done by M.P.H., building on work of J.J.L. Supplementary noise theory was prepared by M.P.H. with assistance from J.J.L. and comments from Y.L. The manuscript was prepared by M.P.H., M.J.S. and J.J.L.

Author Information Reprints and permissions information is available at www.nature.com/reprints. The authors declare no competing financial interests. Readers are welcome to comment on the online version of this article at www.nature.com/nature. Correspondence and requests for materials should be addressed to M.P.H. (mph111@physics.anu.edu.au).

Copyright of Nature is the property of Nature Publishing Group and its content may not be copied or emailed to multiple sites or posted to a listserv without the copyright holder's express written permission. However, users may print, download, or email articles for individual use.